Experiments in Fluids (2023) 64:126
https://doi.org/10.1007/s00348-023-03664-1

RESEARCH ARTICLE

Development of a floating element photoelastic force balance

Bradley McLaughlin[1] · John Lawson[1] · Bharathram Ganapathisubramani[1]

Received: 20 January 2023 / Revised: 19 April 2023 / Accepted: 6 June 2023 / Published online: 1 July 2023

Abstract
We present a floating element force balance design that uses an optical measurement of the force using photoelastic stress analysis. The force sensing element consists of pins embedded in photoelastic polyurethane pads, which generate an internal stress when the floating element is loaded that is observed via a transmission polariscope. A series of known loads and their corresponding fringe patterns allow a calibration matrix to be derived using a polynomial model solved by least squares regression. Finite element analysis (FEA) simulation is carried out to validate the proposed method. The balance then measured a lift curve of the NACA0015 wing at low speed. A comparison of the photoelastic balance and a commercial, 6-axis strain-gauge load cell showed typical differences of less than 6%. This optical approach enables accurate measurements with inexpensive and simple components inside the sensor. This work demonstrates that a photoelastic balance is a simple, inexpensive, and sensitive force transducer.

1 Introduction

The measurement of small aerodynamic forces in the $1-1000$ mN range, such as lift and drag on wind tunnel models at low speeds (Mueller and Jansen 1982) or the net wall shear stress over a floating element (Ferreira et al. 2018), has been historically challenging. Yet, to gain insights into, e.g. reducing fuel consumption caused by bio-fouling and skin-friction drag on ships (Lindholdt et al. 2015), or the low Reynolds number aerodynamics of air vehicles such as UAVs (Mueller and Jansen 1982), such measurements are essential. General indirect methods to measure these forces include control volume analysis and the integration of surface pressure (Baliga and Patankar 1983; Aly 2013). However, in some circumstances, indirect methods are unsuitable because flow-field measurements are inaccessible or because it is infeasible to instrument the model with pressure taps. For turbulent boundary layers, the Clauser chart method provides an indirect way to estimate skin fiction. Still, it is based upon assumptions about the flow, which are not always met (Wei et al. 2005). In contrast, direct methods such as force transducers have the benefit of being independent of flow conditions and do not require assumptions about the flow (Schetz 1997). Although other direct techniques exist for particular configurations, e.g. oil film interferometry over smooth walls (Pailhas et al. 2009), force transducers provide unrivalled choice over model geometry.

A common, direct method of force measurements used in boundary layer studies is the floating element (FE) balance (Pabon et al. 2018; Winter 1979), which traces its origins back to Kempf in 1929 (Kempf 1929). The floating element functions by keeping a "floating" plate, over which the average wall shear stress is to be measured, structurally independent from the rest of the balance and allowing it to move only in plane (Schmidt et al. 1988). A force transducer is coupled to the load on the floating element providing a direct measurement of the (area average) wall shear stress. FE balances are often tailored to the requirements of a given experiment (Ferreira et al. 2018; Schmidt et al. 1988; Winter 1979). As an illustrative example, Ferreira et al. (2018) compute that for a floating element balance with plan area 0.04 m^2 at freestream speeds of up to 25 m/s, the integrated load due to wall shear may be up to ~ 1 N for a rough wall boundary layer and just 50mN in the smooth wall case.

John Lawson and Bharathram Ganapathisubramani have contributed equally to this work.

✉ John Lawson
J.M.Lawson@soton.ac.uk

Bradley McLaughlin
B.T.McLaughlin@southampton.ac.uk

Bharathram Ganapathisubramani
G.Bharath@soton.ac.uk

[1] Aerodynamics and Flight Mechanics Group, University of Southampton, University Rd, Southampton SO17 1BJ, UK

To sense this applied load, strain gauge-based force transducers are by far the most common (Tropea et al. 2007). Such devices are typically very accurate, achieving measurement uncertainties below 0.1% of full scale (Tropea et al. 2007). However, their most significant limitation in this context is their low sensitivity, which makes the direct measurement of $\mathcal{O}$(mN) aerodynamic forces extremely challenging (Ferreira et al. 2018; Mueller and Jansen 1982). In addition, they are sensitive to overload and damage (Yan et al. 2005), and their performance is affected by humidity, and temperature and the repeatability can drop with prolonged use (Bertodo 1959). Furthermore, strain gauges can only measure in one direction. To measure multi-directional loads, complex systems of multiple strain gauges are required (Ştefănescu 2011).

Transducers based on photoelastic principles offer an alternative, optical, non-intrusive means of sensing mechanical loads. Examples include measurement of differential pressure (Martens 1984), torque through a rotating shaft (Chung et al. 1998), point loads (Mukashev et al. 2022; Daniels et al. 2017; Dubey et al. 2007) as well as more complex distributed loads (Dubey et al. 2007) and friction due to slip (Dubey and Crowder 2006). In all these examples, a mechanical load is transferred to a photoelastic material, which exhibits stress-induced birefringence. The stress field can be visualised using a polariscope using standard techniques (Phillips 1998), allowing optical measurement of the load. The resultant photoelastic fringe patterns can be recorded using inexpensive colour cameras (Chung et al. 1998; Dubey et al. 2007; Mukashev et al. 2022) and interrogated to infer the load. In an aerodynamic context, the concept was recently employed by Etter et al. (2022) to measure wind-speed from aerodynamic loads exerted on a whisker-like structure embedded in a photoelastic material. However, to date, photoelasticity based sensors have been infrequently used and have not been applied to make direct force measurements in an aerodynamic application.

In the case of floating element balances, photoelastic force transducers are attractive because the load can be sensed optically and non-intrusively using inexpensive components. The mechanical design can also be simplified. This allows a new design space to be explored, e.g. to create an array of several, inexpensive balances, or to measure multiple components of applied force or moment. It also allows the possibility of creating more easily sealed designs, since feedthroughs for sensor electronics are not required. This is desirable if the gap around the floating element is to be filled with liquid to mitigate horizontal buoyancy forces created by pressure gradients (Hirt et al. 1986), which are a significant source of skin friction measurement error (Brown and Joubert 1969; Hirt et al. 1986). We have previously explored this design possibility (Ferreira et al. 2018), but rejected it due to the practical difficulties of containing the liquid around the other balance components.

Although photoelastic force transducers offer some desirable characteristics for use in aerodynamic applications, the main difficulty to overcome is their limited sensitivity and accuracy. For instance, Mukashev et al. (2022) report a typical measurement uncertainty of around 6% of full scale load (8 N) in the measurement of point loads. Similarly, Dubey et al. (2007) report typical measurement uncertainties of around 3–4% of full scale load (25 N). The full-scale load in these examples is still an order of magnitude larger than required for wall shear-stress sensing (Ferreira et al. 2018). Therefore, to become competitive with strain-gauge based transducers, new designs which improve both the sensitivity and accuracy are required. To achieve the latter, a better understanding of the main error sources is required.

In this paper, we demonstrate a proof-of-concept design of floating element force balance that uses a photoelastic element to sense millinewton scale forces and quantify the main sources of measurement uncertainty using finite element analysis simulations and wind tunnel tests. This represents a first-step in exploring the design space of FE balances based on photoelastic transducers, and achieves a significant improvement in absolute measurement uncertainty over previous, comparable sensors (Dubey and Crowder 2006; Dubey et al. 2007; Mukashev et al. 2022). The sensing element functions by capturing images of the photoelastic patterns created by concentrated point-loads applied to a set of polyurethane pads, which secure the floating element. These patterns are then calibrated against a polynomial model. The concept is explored through finite element analysis (FEA) simulations, which allow us to investigate the main sources of measurement error in our design and predict its performance. We then test our design experimentally via low-speed wind tunnel measurements of the lift of a NACA0015 aerofoil mounted on the FE balance. These are compared to replicate measurements taken by a commercially available strain-gauge based load cell.

The paper is structured as follows. Section 2 outlines the design of the balance and the operating principle of force sensing. In Sect. 3, we introduce our finite element analysis simulation and document the results of tests on synthetic images. In Sect. 4, we document our wind tunnel testing methodology and present the results of our wind tunnel testing in Sect. 5. We provide conclusions in Sect. 6.

2 Balance design and calibration method

Photoelasticity is an optical method of stress and strain analysis. It takes advantage of a mechanical property called stress-induced birefringence, which many transparent polymers possess (Phillips 1998). Birefringence occurs when

light waves travelling through a material are split into two components according to their polarisation, which experience different refractive indices. Under planar stress perpendicular to the optical axis, stress-induced birefringence creates "fast" and "slow" axes in the material, causing the material to act as a temporary wave-plate with a stress-dependent phase shift. The angular phase shift Δ is related to the stress by the stress-optic law (Phillips 1998):

$$\Delta = \frac{2\pi C t}{\lambda}(\sigma_1 - \sigma_2) \tag{1}$$

where C is the stress-optic constant (a material property), t is the thickness of the sample along the optical axis, λ is the wavelength of the incident light, and σ_1 and σ_2 are the principal stresses (ordered $\sigma_1 > \sigma_2$) in the plane perpendicular to the optical axis. Equation 1 shows that the phase shift is directly proportional to the difference in the principal stresses. It is this relationship that allows the photoelastic force balance to function.

Figure 1 shows the cross-section of one of the photoelastic sensing elements. An upper PMMA acrylic plate, acting as the floating element, transfers an aerodynamic load to a slender pin embedded in a polyurethane pad, which acts as the photoelastic material. Two circular polarising films, each consisting of a linear polariser and quarter wave-plate, are arranged on either side of the pad to create a circular polariscope. The polariser is backlit by white light from LED strips around the edge of the top PMMA plate, which acts as a light pipe. A USB camera is placed directly underneath the pad to take images of the photoelastic pattern in the pad.

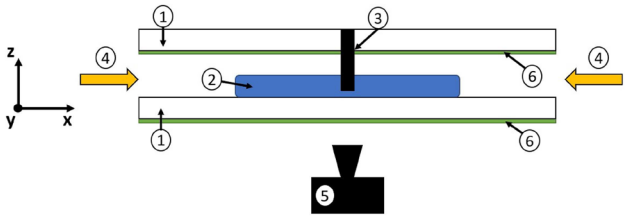

Fig. 1 Cross-section of a photoelastic force balance element. A slender pin (3) creates a high-stress region in a photoelastic, polyurethane pad (2) as a load is applied to the upper floating element. The stress field is visualised using a circular polariscope (6), which is back-illuminated by white LED light (4) guided to the sample through the transparent PMMA sheets (1), and is imaged from below with a camera (5)

Figure 2 shows an example of the fringe pattern observed in a single pad. The stress concentration generated by transferring the load to the slender pin is essential to achieving a large sensitivity. By doing so, we generate a large photoelastic response with a small force, unlike previous approaches (Dubey and Crowder 2006; Dubey et al. 2007; Mukashev et al. 2022) where the applied load is distributed over a much larger region of photoelastic material. Even when the pad is unloaded, there is a pronounced fringe pattern due to internal stresses from the insertion of the pin into the pad. Initially, attempts were made to minimise this. However, as we will discuss in Sect. 3, our FEA study highlighted that this pre-loading is essential to measuring the direction of the applied load. There are additional practical considerations to ensure a clear fringe pattern. The colour temperature of the LED light (6000 K) was chosen to ensure even illumination intensity across colour components. A matte white background (in this case, correction fluid) is used to ensure homogeneous, white backlighting. It was also helpful to paint the other internal components black to minimise external light and reflections.

To measure the applied load from colour fringe pattern images, a least squares fit to a fifth order polynomial model is used. The fringe pattern image can be represented as a column vector $\boldsymbol{y}$ with $N = 3n_{px}$ elements, corresponding to the red-green-blue intensity of each pixel. The polynomial model $\boldsymbol{y}^\star$ of the image is written

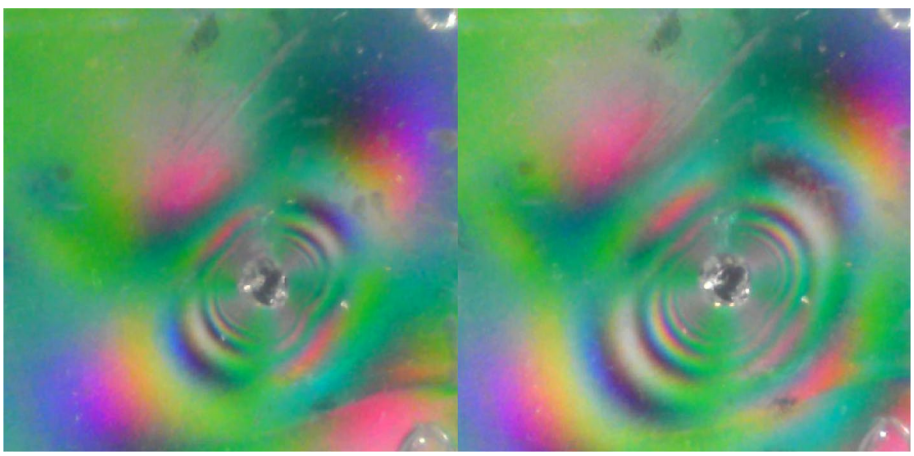

Fig. 2 Example of the photoelastic fringe pattern for an unloaded pad (left) and under a 0.5 N horizontal load (right)

$$\boldsymbol{y}^{\star} = \sum_{n=0}^{5} \boldsymbol{c}_n F^n = \boldsymbol{C}\boldsymbol{x} \tag{2}$$

where F is the applied axial load and vectors $\boldsymbol{c}_n \in \mathbb{R}^{3n_{px}}$ are unknown calibration coefficients. For convenience, we write these in terms of the matrix $\boldsymbol{C} = \{\boldsymbol{c}_n\}_{n=0}^{5}$ whose columns correspond to the coefficients $\boldsymbol{c}_n$, and a vector $\boldsymbol{x} = [F^0 \dots F^5]$ of polynomial terms. To calibrate the sensor, a $N \times K$ matrix $\boldsymbol{Y} = \{\boldsymbol{y}_i\}_{k=1}^{K}$ is built up of K calibration images recorded at known loads F_k. To obtain the coefficients $\boldsymbol{C}$, we solve $\boldsymbol{Y} \approx \boldsymbol{C}\boldsymbol{X}$ in the least-squares sense for $\boldsymbol{C}$, where $\boldsymbol{X} = \{\boldsymbol{x}_k\}_{k=1}^{K}$ is a $K \times 6$ matrix of polynomial terms. The least-squares solution is given by $\boldsymbol{C} = \boldsymbol{Y}\boldsymbol{X}^{\mathrm{T}}\left(\boldsymbol{X}\boldsymbol{X}^{\mathrm{T}}\right)^{-1}$. The calibration matrix $\boldsymbol{C}$ can now be used to determine the unknown loads to a given image $\boldsymbol{y}$. A non-linear least squares fit is used based on (2), which finds the value of F that minimises the $\mathbb{L}_2$ norm error $\|\boldsymbol{y} - \boldsymbol{y}^{\star}\|_2$ between the model and the image.

An engineering drawing of the force balance used in the wind tunnel tests is shown in Fig. 3. It consists of a 220×220 mm^2 square frame, laser cut from 5 mm thick PMMA acrylic sheet, with the bottom and top plates cut from the same material. The bottom plate was cut to fit tightly inside the frame, while the top plate was cut with rounded corners and a 1 mm clearance to avoid contact with the sides of the frame. The floating element sits upon four polyurethane pads, located at the midpoint of each edge and connected via 0.7 mm diameter pins. The pads are of approximately $10 \times 10 \times 2$ mm^3 cuboidal shape with a shore hardness of 65A and a Young's Modulus of 2.42 MPa. There is a 1mm clearance between the top of the pads and the top plate. While the properties of the polyurethane may change with time, the calibration accounts for this issue. Our experimental protocol has been to complete a calibration at the start of a given experiment which is repeated weekly. This practice has allowed for experiments over three weeks or more with no noticeable reduction in accuracy with time.

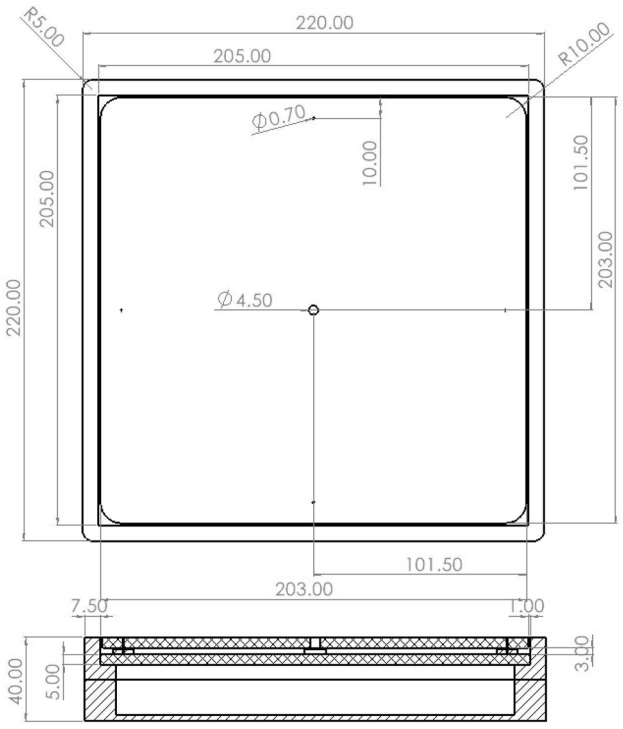

Fig. 3 Engineering drawing of photoelastic force balance

3 Tests on synthetic data

To predict the performance of this design, and to validate the calibration method, we conducted FEA simulations of a single pad under various loadings. The FEA model is a simplified, 2D version of the sensing element, i.e. a square pad with side length $w = 10$ mm and a circular hole of diameter $d = 0.7$ mm. The geometry is shown in Fig. 4. The dimensions were chosen to match the physical balance and the simulation assumed a Young's Modulus of 2.5 MPa and a Poisson's ratio of 1/3 to match the actual pad's properties. The pad was loaded with a uniform, horizontal surface traction force F and radial pressure P at surface S1. A no-displacement boundary condition was applied at the edges of the pad, S2.

The FEA was conducted in MATLAB using the in-built static plane stress modeling package. The maximum edge size of the mesh was 1/12 of the pin diameter. More refined meshes were tested, but the change in solution was minimal and significantly increased processing time. The solution was then interpolated onto a regular grid with 256×256 elements. We modelled the response of a circular polariscope as (Phillips 1998)

$$I(x, y) = I_0 \cos^2\left(\frac{\Delta}{2}\right) \tag{3}$$

where $I(x, y)$ is the intensity after passing through the polariscope, $I_0 = 1$ is the initial intensity, and $\Delta(x, y)$ is the relative retardation of the incident light. This is performed at wavelengths $\lambda = 630, 532$ and 465 nm, simulating red, green and blue channels in a colour image. The stress-optic constant of polyurethane was taken to be $C = 3.5 \times 10^{-9}$ Pa^{-1} (Aben and Guillemet 1993). Images were discretised to 256 levels over the interval [0, 1], which simulates acquisition using an 8-bit image sensor.

Figure 4 shows an example of the synthetic fringe pattern under different loadings. The fringe pattern resulting from a pure horizontal load, shown in Fig. 4a, is symmetric about the axis of the applied force. It is therefore not possible to determine the direction of the load. In order to measure direction as well as magnitude, an asymmetry

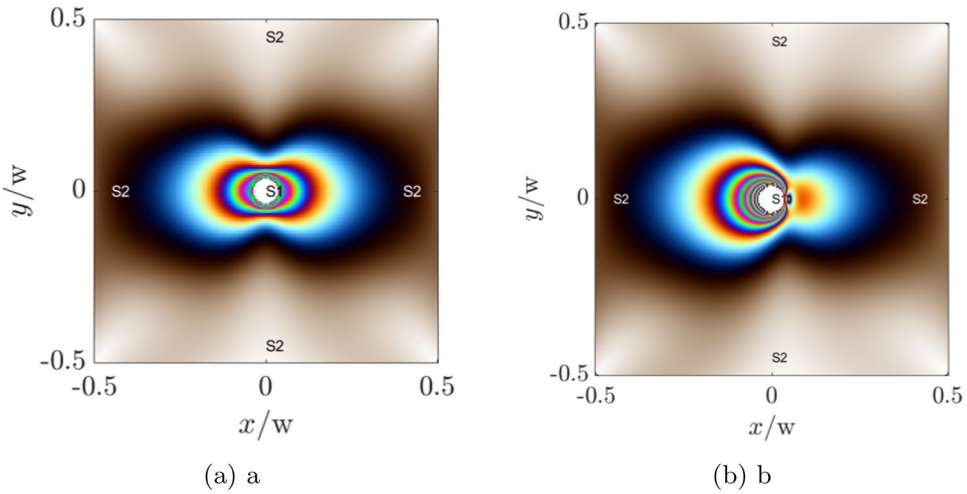

Fig. 4 Simulated fringe pattern response to a load in the $+x$ direction without pre-loading (left) and with radial pressure pre-load (right). The symmetry of the principal stress field $(\sigma_1 - \sigma_2)$ is broken by the radial pre-load, allowing the direction of the load to be inferred

must be introduced into the principal stress field. This can be achieved by applying a pre-load. Three types of pre-loading conditions were explored. The first was a pre-load in the direction of the measured force (x-direction), the second perpendicular to the measured force (y-direction), and the last case was an applied pressure force from the central hole (radial stress). Figure 4b shows the same applied force as 4a but with the third type of pre-loading, radial stress. With apparent asymmetry in Fig. 4b, direction information is now contained within the fringe pattern.

To calibrate our virtual sensor, $K = 21$ fringe patterns were obtained for applied loads of $F = -1$ N … 1N in steps of 0.1 N and used to construct a calibration (2). Following this, fringe patterns were obtained for loads between $F = -1 \ldots 1$ N in increments of 0.01 N to test the model.

3.1 Ideal loading and necessary pre-load

Figure 5 shows the response of virtual sensor calibrated with the 5th order polynomial model (2). Because these data contain no random error, deviations in the calibrated response are due to systematic error introduced by the calibration model. As expected, without pre-loading, the magnitudes of the load can be captured, but direction cannot. Furthermore, the systematic error is very large at small loads. By pre-loading in the direction of the measured force, this ambiguous region can be offset, but not eliminated. By applying a pre-load in the direction perpendicular to the measured force, the ambiguity can be eliminated, but significant systematic errors remain at the largest loads. This approach could have severe limitations in practice, as the calibrated response may become sensitive to off-axis loads. This directional sensitivity can be avoided by pre-loading with a radial stress with comparable systematic error.

The required magnitude of this radial pre-stress to ensure accurate measurements remains unknown. To determine the

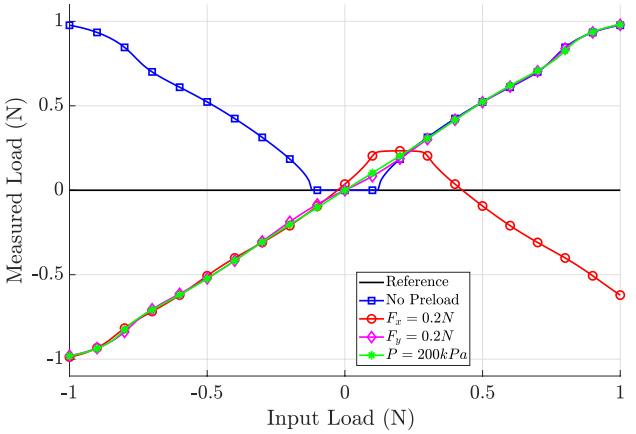

Fig. 5 Tests on synthetic data showing the effect of introducing a pre-load force or radial pressure upon the directional sensitivity of the photoelastic sensor

magnitude of this pre-stress, we first define a non-dimensional radial pressure as,

$$\hat{P} = \frac{\pi t d P}{F_{fs}} \tag{4}$$

which normalises the radial pressure P against the characteristic shear stress $F_{fs}/(\pi t d)$ in the element at full scale. Here F_{fs} is the full-scale load, t is the thickness of the pad, and d is the diameter of the hole. Figure 6 shows the systematic error of the calibration for $\hat{P} = 0.5, 1, 1.5, 2, 4, 8$. As $\hat{P}$ increases, the systematic error in the measurements is reduced. Beyond $\hat{P} = 2$, the improvement in systematic error is negligible.

Equation (2) essentially obtains a Taylor series expansion of the combined polariscope (3) and principal stress field response to a change in the applied loading, F. Therefore, systematic errors are introduced into the force measurement as the polynomial model deviates from the

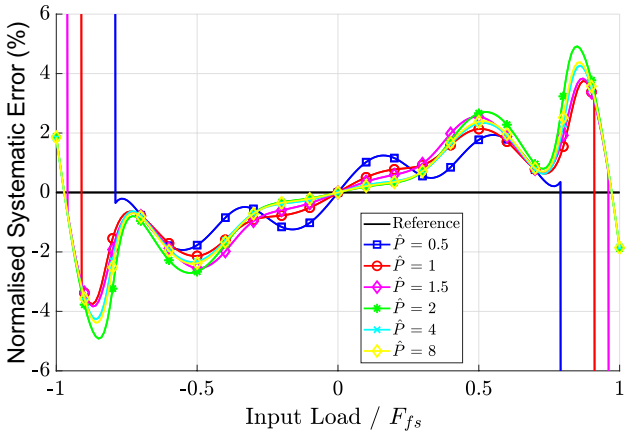

Fig. 6 Systematic calibration error, normalised by full scale load F_{fs}, shown for different values of radial pre-load $\widehat{P}$. For $\widehat{P}$ of 0.5 and 1, the error near the full scale and close to zero is large. For $\widehat{P} \geq 2$, increasing the radial pre-load results in no significant improvement in systematic error

non-linear photoelastic response of the element. As the calibrated range is increased, the sensor response at full scale is increased and easier to detect, but the suitability of Eq. (2) may vary. Therefore, we examined the effect of changing the full scale load used for the calibration whilst keeping the radial pre-load dimensionally similar $\widehat{P} = 2$. Figure 7 shows the normalised systematic error for full scale load $F_{fs} = 0.5, 1, 1.5$ N. In all cases, the method accurately measured magnitude and direction. Systematic error reduces with the reduction of the full scale load.

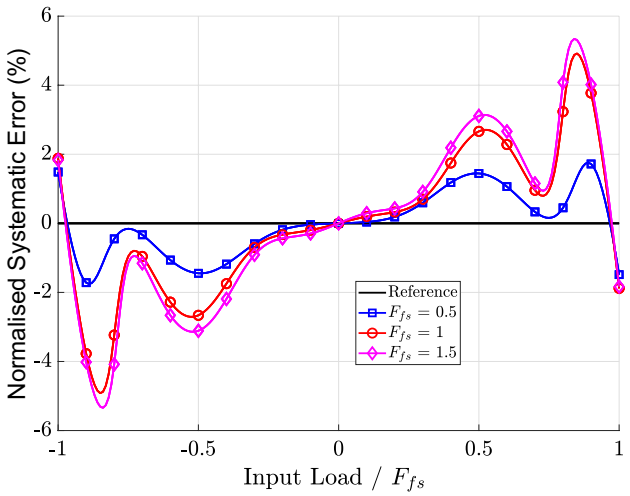

Fig. 7 Dependence of the systematic error (normalised by full scale) upon the full-scale calibration range F_{fs}, for $\widehat{P} = 2$. Smaller full scale loads result in a lower systematic error

3.2 Effect of noise

To understand the effect of image noise on the measurement, zero-mean Gaussian noise was added to the synthetic images with a standard deviation $\sigma = 0.071$, i.e. a signal to noise ratio of $\sim$ 23dB, corresponding to a strong random noise source. The calibration matrix was built using images without noise for $\widehat{P} = 2$ and $F_{fs} = 1$ N. Figure 8 shows that the noise contribution is negligible in comparison to the systematic error, despite the strong noise. As an example, at $F = 0.6$ N, the systematic error in the measurement is 21.5 mN, whilst the standard deviation of the random error is 0.2 mN.

3.3 Directional dependence

To explore the ability of the balance to separate loads in cross directions, a calibration was made as above ($F = -1$ N … 1N in steps of 0.1 N) with no load in the Y direction. Test images were simulated between $F_x = -1$ N … 1N in steps of 0.01 N with a radial pre-load of $\widehat{P} = 2$ and an additional load $F_y = 0$ N … 1N in steps of 0.2 N. The systematic error in these measurements is shown in Fig. 9. It is apparent that a simple 1D polynomial calibration is not sufficient to measure the axial load accurately when under a general 2D loading. In principle, this effect could be accounted for by performing a 2D calibration using a generalised 2D polynomial model. However, for small traverse loads F_y, the loss in accuracy due to transverse loading is minimal. The error in the $F_y = 0.2N$ case (i.e. a transverse load of 20% of full scale) is still less than 5% at all points.

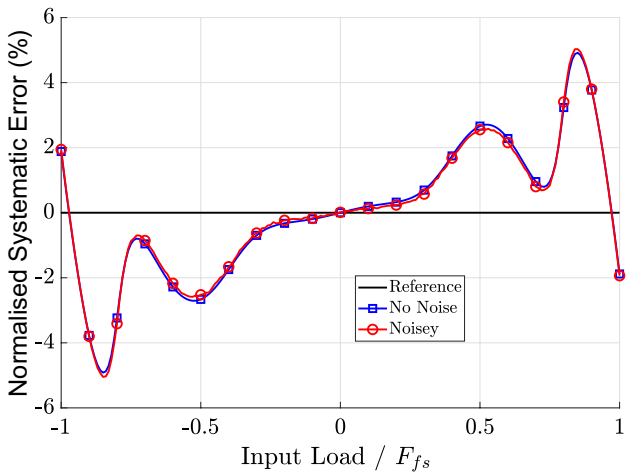

Fig. 8 Sensitivity of systematic error (normalised by full-scale load) to Gaussian image noise with a signal to noise ratio of 23 dB, full scale $F_{fs} = 1$ N and $\widehat{P} = 2$. The effect of strong image noise is negligible

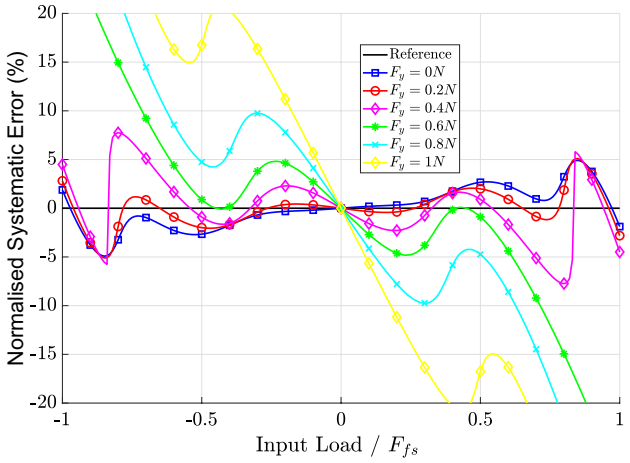

Fig. 9 Sensitivity of the systematic error, obtained for a 1D calibration, to varying transverse loadings with $F_{fs} = 1$ N and $\widehat{P} = 2$

To summarise, tests on synthetic data validate the polynomial fitting procedure and demonstrate the feasibility of measuring forces with a photoelastic sensor. The FEA indicates that ideally, there should be a pre-load radial stress applied of a size that results in a $\widehat{P} \geq 2$. This analysis also shows that while the error is slightly larger towards zero, the method is robust to noise. Further, the polynomial regression method is accurate to single-direction loading and can handle traverse loads up to $F_y \approx 20\%$ of full scale. A multivariate polynomial regression or a more advanced data-driven method would be needed to measure two-directional loading or cross-loads on similar scales. The simple polynomial regression was deemed to be acceptable for the experimental validation presented here where the lift force measurement of a wing is carried out. Here, the drag force will be significantly smaller than the expected lift force.

4 Experimental demonstration

The sensitivity of the photoelastic force balance was tested in practice by measuring the aerodynamic loads on a 2D, NACA0015 wing section at low speed ($\mathrm{Re} = 4 \times 10^5$ and 5.7×10^5). As a comparison, we also characterised the performance using a commercial ATI mini40 strain-gauge based load cell. Measurements were conducted in an open-loop, low-speed, blow-down wind tunnel at the University of Southampton, previously characterised in Bleischwitz 2016. Although measuring skin friction is the intended application, we choose this simpler configuration for reasons of practicality and time constraints in using our larger, boundary layer wind tunnel facility (BLWT). However, the loads in both scenarios are comparable. For instance, based on a rough surface of staggered cubes with skin friction coefficient

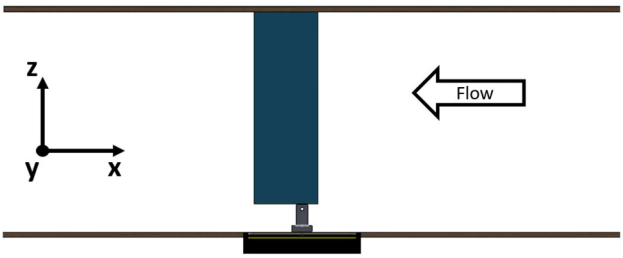

Fig. 10 CAD model of the experimental set-up inside of the wind tunnel

$C_f = 8.5 \times 10^{-3}$ (Ferreira et al. 2018), we estimate the drag on our floating element balance would be between 20 and 413 mN for typical free-stream speeds in the BLWT between 10 and 45 m/s. In the present measurements, the largest lift force measured is around 771 mN.

The experimental setup is shown in Fig. 10. The balance was fared into the floor of the tunnel, which has a cross-section of 43×48 cm, and the wing affixed to the floating element using an optical post holder. The wing model is a foam cut NACA0015 section supported by a carbon fiber rod through the quarter chord, with a chord length of $c = 12$ cm, a span of $s = 36$ cm and aspect ratio $\mathcal{AR} = 3$. In the comparison experiment, the ATI sensor was also fared into the tunnel floor. This reference sensor has a resolution of $1/200$ N in the lift- and drag- axes and 20 N full scale. The freestream velocity U_∞ was determined using a Pitot tube to measure the dynamic pressure $\Delta p = \frac{1}{2}\rho U_\infty^2$ using a FCO560 digital manometer, which has an accuracy of ± 0.23Pa. Two free-stream speeds U_∞ were tested, 5 m/s and 7m/s, resulting in chord-based Reynolds number of $\mathrm{Re} = 4 \times 10^5$ and 5.7×10^5 respectively. The wing was tested over a range of angle of attack $\alpha = -14 \ldots 12°$ in steps of 2°.

The balance was calibrated for forces applied along the lift axis, as shown in Fig. 10. The calibration was completed inside the wind tunnel where the wing test would occur. Point loads were applied at the half-span of the wing via known weights suspended on a monofilament Nylon fishing line using a Pasco ME-9450 low-friction pulley with an effective coefficient of friction of 7×10^{-3} (Ferreira et al. 2018). We have observed that the balance response is sensitive to the moment arm, i.e. the height at which the load is applied, so the loads were applied at the approximate aerodynamic centre. The masses ranged from -100 to 100 g in steps of 10 g, and the weight of the line was assumed to be negligible. For each load, a video was recorded at 7.5 frames/s for 40s: 10s unloaded, 20s loaded, and 10s unloaded. The unloaded period allowed the background image to be removed to account for the internal stress of the pad. An average image $\boldsymbol{y}$ was found for each video, corresponding to the difference between the loaded

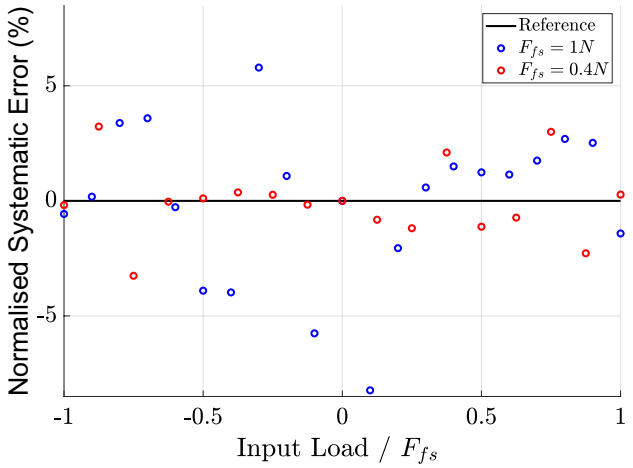

Fig. 11 Systematic error normalized by F_{fs} for two different physical calibrations

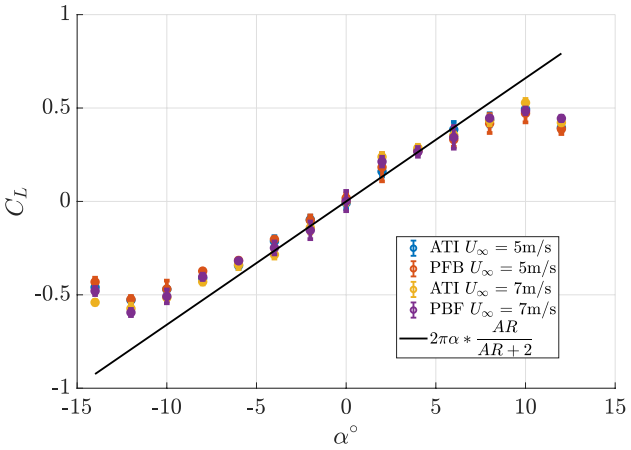

Fig. 12 Comparison of lift coefficient C_L of wing model determined from strain-gauge based ATI mini40 sensor and photoelastic balance at free-stream speeds $U_\infty = 5$ m/s and 7 m/s over a range of angle of attack α. The black line shows the semi-empirical lift-curve slope prediction (5) for an $\mathcal{AR} = 3$ wing below stall

and unloaded states. Frames were not included in the averaging process around the application and removal of the load to avoid any transients. This method created an image showing the average change in the fringe pattern due to the application of the load. The procedure resulted in $K = 21$ images, one for each applied load, which were used to obtain a calibration as in Sect. 2.

Figure 11 shows the systematic error in the experimental calibration, which was obtained by applying the calibration model to the calibration input images it was derived from. The maximum systematic error is around 8% of full scale $F_{fs} = 1$ N and shows no obvious trend. When the calibration was repeated over a smaller range of masses $-40 \ldots 40$ g in 5g increments, we observe that the systematic error is lower in both relative and absolute terms ($< 3.3\%$ of full scale), consistent with our observations in Fig. 7. This shows that the measurement range of the balance can be tailored to operate over different scales. We also note that the systematic error observed is comparable in magnitude to our FEA simulations in Fig. 7. The calibration of $F_{fs} = 1$ N is used in the subsequent experiments presented here.

5 Results

Measurements of lift for the NACA 0015 aerofoil were taken over a period of six days, with the calibration for the photoelastic balance performed on the first day. Six repeats of the lift measurements as a function of the angle of attack were performed for the ATI sensor, whilst three repetitions of the measurement were taken for the photoelastic balance. A comparison of the $C_L - \alpha$ curves obtained using the ATI and photoelastic sensors is shown in Fig. 12. A common semi-empirical approximation of the lift-curve slope of a finite, symmetric aerofoil

$$C_L = 2\pi\alpha\left(\frac{\mathcal{AR}}{\mathcal{AR}+2}\right) \tag{5}$$

which is appropriate for slender, small aspect ratio, rectangular planform wings below stall (John D. Anderson 2016) is also shown.

Figure 12 shows that the lift-curve of all four data sets collapses and follows the expected theoretical lift-curve (5) at small angles of attack. Both techniques capture the angle of maximum lift (and stall) at the same angle of attack. A standard uncertainty propagation and uncertainty budget was performed for the lift coefficient measurements, detailed in Appendix A. The error bars in Fig. 12 show the uncertainty in the measurement to 95% confidence interval. The largest source of uncertainty comes from the repeatability of the lift. It is remarkable that, over six days of aerodynamic testing, the photoelastic force balance calibration is stable enough to provide uncertainty comparable to a commercial sensor which is two orders of magnitude more expensive. The most significant difference between the ATI and the photoelastic sensors occurs at the smallest angles of attack, where the forces measured are the smallest. The RMS error between the ATI and photoelastic sensors for the $U_\infty = 5$m/s case was 16 mN and 36mN for the 7m/s case. The average discrepancy between the two was 4.8% and 6.8% at 5 and 7m/s respectively, for an overall "average" discrepancy of 5.9%. In dimensional

Table 1 Example uncertainty budget in lift coefficient C_L for the photoelastic force balance at $U_\infty = 5\text{m/s}$ and $\alpha = 6°$

Measured quantity	Accuracy	Sensitivity value	Uncertainty contribution (u)
Lift (L)	0.0143 N	1.518 N^{-1}	0.0217
Temperature (T)	0.1 K	0.00113 K^{-1}	6.5×10^{-5}
Atmospheric Pressure (p_{atm})	100 Pa	3.2×10^{-6} Pa^{-1}	1.8×10^{-4}
Velocity (U_∞)	0.06 m/s	0.133 s/m	0.00461
Area (A)	0.001 m^2	7.681m^{-2}	0.00443
Combined uncertainty			0.0227

Table 2 Example uncertainty budget in lift coefficient C_L for the ATI Mini 40 sensor at $U_\infty = 5\text{m/s}$ and $\alpha = 6°$

Measured quantity	Accuracy	Sensitivity value	Uncertainty contribution (u)
Lift (L)	0.0137 N	1.518 N^{-1}	0.0208
Temperature (T)	0.1 K	3.2×10^{-5} K^{-1}	1.9×10^{-6}
Atmospheric Pressure (p_{atm})	100 Pa	1.1×10^{-7} Pa^{-1}	6.2×10^{-6}
Velocity (U_∞)	0.06 m/s	0.154 s/m	0.00534
Area (A)	0.001 m^2	8.89 m^{-2}	0.00514
Combined uncertainty			0.0221

terms, the largest lift force measured is approximately 771 mN. The consistency of these results demonstrates that the photoelastic force balance can reliably measure millinewton scale aerodynamic loads with comparable performance to a commercial strain-gauge-based sensor.

Example uncertainty budgets for the lift coefficient obtained for the PFB and the ATI sensor are presented in Tables 1 and 2, respectively. The uncertainty of the two sensors is very similar, both in total contribution and in how the contribution is distributed among the sources of error. The budget confirms that the largest source of uncertainty comes from the repeatability of the lift. The area and the velocity had a moderate effect, while the temperature and pressure readings had minimal impact on the measurement of C_l.

6 Conclusions

In this paper, we have presented the proof-of-concept of a floating element force balance design based on the principles of photoelasticity to measure small (< 1 N) aerodynamic loads with typical measurement error as low as 16 mN. This high sensitivity is achieved by concentrating the load from the floating element onto slender pins embedded in a photoelastic material, creating a stress concentration which induces a large photoelastic response. A fifth-order polynomial model is then calibrated to model fringe pattern images generated by loading the balance in one dimension, which can be used to determine the applied load from the fringe patterns.

Finite element analysis was used to predict the performance of the design and validate the calibration method. The FEA shows that some pre-loading of the element is essential to provide directional sensitivity. This can be effectively achieved by the radial stress created around the pin as it is inserted into the photoelastic material. Systematic errors are introduced into the force measurement as the polynomial model deviates from the true, nonlinear photoelastic response of the element. The systematic errors are the main source of measurement error: synthetic images contaminated with strong random noise (signal to noise ratio 23 dB) show that random error introduced by image noise is two orders of magnitude smaller than the systematic error. The absolute and relative magnitude of the systematic errors, in comparison to the full scale load, can be reduced by calibrating over a smaller range. This observation is replicated in subsequent experimental tests. Systematic errors can also be induced by off-axis loads. A simple, 1D polynomial calibration model results in systematic errors below 5% of full scale provided the off-axis load is below 20% of full scale. Under a more general 2D loading, the 1D polynomial calibration model fails. A more general multivariate polynomial regression model or more advanced data-driven method would be needed to measure 2D loading or off-axis loads on similar scales.

We tested our design experimentally in a low-speed wind tunnel by measuring the lift force on a 2D NACA0015 aerofoil mounted on the floating element. We compared these measurements to replicate measurements obtained using a commercially available ATI mini40 strain-gauge based load cell. The results from the PFB and ATI load cell are within 6% of each other. In absolute terms, the RMS discrepancy between the two was around $16 - 36$ mN, which is comparable to the repeatability of the measurement itself. This proof-of-concept shows the technique is suitable to measure the forces expected on rough walls in our boundary layer wind tunnel facility.

Although the systematic error at full scale is still larger than well-optimised strain-gauge based FE balances (Ferreira et al. 2018), the balance presented here represents a first-step in applying photoelasticity based sensors to measure small

loads. It has the advantages of being a non-intrusive optical measurement, having an inexpensive and simple mechanical design with no moving parts or electrical components in the sensor. This opens up new measurement possibilities for future research, e.g. to create an array of several, inexpensive balances or to fill the cavity around the the floating element with liquid to reduce horizontal buoyancy effects. Furthermore, the sensitivity of our photoelastic sensor to off-axis loads could be exploited to measure multiple components of force, which we have confirmed in initial tests using a 2D polynomial calibration. We have also found that the balance is also able to measure unsteady forces (McLaughlin et al. 2023). A simple calculation based on the FEA-modelled stiffness and mass of our current design suggests the natural frequency is around 50Hz, which offers the prospect of time-resolved sensing up to $O(10\ \mathrm{Hz})$. Future research should quantify the temporal response of such photoelastic sensors.

A Uncertainty analysis

The standard uncertainty in the lift coefficient $C_l = 2L/(\rho U_\infty^2 A)$ is obtained from uncertainty propagation (Kirkup and Frenkel 2006), where $A = sc$ is the wing planform area and the air density $\rho = p_{atm}/RT$ is calculated from the ideal gas equation, where $R = 287.05\mathrm{Jkg}^{-1}\mathrm{K}^{-1}$ is the specific gas constant for air, p_{atm} is the atmospheric pressure, and T is the ambient temperature. The standard uncertainty u_{C_l} therefore given in terms of the uncertainty of the measurands u_X as

$$u_{C_l}^2 = \left(\frac{\partial C_l}{\partial L}u_L\right)^2 + \left(\frac{\partial C_l}{\partial T}u_T\right)^2 + \left(\frac{\partial C_l}{\partial P}u_P\right)^2 + \left(\frac{\partial C_l}{\partial U}u_U\right)^2 + \left(\frac{\partial C_l}{\partial A}u_A\right)^2. \tag{6}$$

The uncertainty in the lift measurement and in the free-steam velocity were found from the repeatability of the measurements across three runs. The uncertainty of the temperature and of the area where taken form the gradation of the temperature probe and the ruler used to measure the wing dimensions, having a resolution of 0.1° and 1mm respectively. The pressure was taken from a local weather station accurate to 100Pa. Example uncertainty budgets for the lift coefficient obtained for the PFB and the ATI sensor are presented in Tables 1 and 2 respectively.

Author Contributions BM - Data Collection, Data Analysis, Figure Preparation, Writing - Original Draft; JL - Conceptualisation, Data analysis, Review and Editing; BG - Funding, Data Analysis, Review and Editing.

Funding The authors are grateful for financial support from the Engineering and Physical Sciences Research Council (Ref No: EP/S013296/1 and EP/W026090/1).

Data Availability Pertinent data for this paper are available at https://doi.org/10.5258/SOTON/D2675.

Declarations

Conflict of interest The authors report no conflict of interest.

Ethical approval Not applicable.

References

Aben H, Guillemet C (1993) Two-dimensional photoelasticity. Photoelasticity of glass. Springer, Berlin, pp 69–78

Aly AM (2013) Pressure integration technique for predicting wind-induced response in high-rise buildings. Alex Eng J 52(4):717–731

Baliga BR, Patankar SV (1983) A Control Volume Finite-element Method for Two-dimensional Fluid Flow and Heat Transfer. Numerical Heat Transfer 6(3):245–261

Bertodo R (1959) Development of high-temperature strain gauges. Proc Inst Mech Eng 173(1):605–622

Bleischwitz R (2016) Fluid-structure interactions of membrane wings in free-flight and in ground-effect. PhD thesis, University of Southampton

Brown KC, Joubert PN (1969) The measurement of skin friction in turbulent boundary layers with adverse pressure gradients. J Fluid Mech 35(4):737–757

Chung D, Merat FL, Discenzo FM, Harris JS (1998) Neural net based torque sensor using birefringent materials. Sens Actuators A 70(3):243–249

Daniels KE, Kollmer JE, and Puckett JG (2017) Photoelastic force measurements in granular materials. Rev Sci Instrum 88(5)

Dubey VN, Crowder RM (2006) A dynamic tactile sensor on photoelastic effect. Sens Actuators A 128(2):217–224

Dubey VN, Grewal GS, Claremont DJ (2007) Load extraction from photoelastic images using neural networks. Exp Mech 47(2):263–270

Etter E, Mulleners K, and Ayancik F (2022) Application of transmission photoelasticity in visualizing fluid-structure interactions. In: 20th international symposium on application of laser and imaging techniques to fluid mechanics, Lisbon, Portugal

Ferreira MA, Rodriguez-Lopez E, Ganapathisubramani B (2018) An alternative floating element design for skin-friction measurement of turbulent wall flows. Exp Fluids 59(10):155

Hirt F, Zurfluh U, Thomann H (1986) Skin friction balances for large pressure gradients. Exp Fluids 4(5):296–300

John D, Anderson J (2016) Fundamentals of aerodynamics

Kempf G (1929) Neue ergebnisse der widerstandsforschung. Werft, Reederei, Hafen, pp 234–239

Kirkup L, Frenkel RB (2006) An introduction to uncertainty in measurement. Cambridge University Press, Cambridge

Lindholdt A, Dam-Johansen K, and Olsen SM (2015) Effects of biofouling development on drag forces of hull coatings for oceangoing ships: a review. J Coat Technol Res

Martens G (1984) Measurement of pressure by photoelastic effects. Sens Actuators 6(3):181–190

McLaughlin B, Lawson J, and Ganapathisubramani B (2023) Measuring instantaneous forces with a photoelastic force balance. AIAA SCITECH 2023 forum, p. 1937

Mueller T, Jansen JRB (1982) Aerodynamic measurements at low Reynolds numbers. In: 12th aerodynamic testing conference, Reston, Virigina. American Institute of Aeronautics and Astronautics

Mukashev D, Zhuzbay N, Koshkinbayeva A, Orazbayev B, Kappassov Z (2022) PhotoElasticFinger: robot tactile fingertip based on photoelastic effect. Sensors 22(18):1–14

Pabon RJ, Ukeiley L, Sheplak M, Barnard Keane C (2018) Characteristics of turbulent boundary layer large scale motions using direct fluctuating wall shear stress measurements. Phys Rev Fluids 3(11):114604

Pailhas G, Barricau P, Touvet Y, Perret L (2009) Friction measurement in zero and adverse pressure gradient boundary layer using oil droplet interferometric method. Exp Fluids 47(2):195–207

Phillips JW (1998) Photoelasticity. Experimental Stress Analysis, Urbana

Schetz JA (1997) Direct measurement of skin friction in complex fluid flows. Appl Mech Rev 50(11S):S198–S203

Schmidt M, Howe R, Senturia S, Haritonidis J (1988) Design and calibration of a microfabricated floating-element shear-stress sensor. IEEE Trans Electron Devices 35(6):750–757

Ştefănescu D (2011) The basic circuit for strain gauge force transducers. In: Handbook of force transducers. Springer

Tropea C, Yarin AL, Foss JF (eds) (2007) Handbook of experimental fluid mechanics. Springer, Berlin

Wei T, Schmidt R, McMurtry P (2005) Comment on the Clauser chart method for determining the friction velocity. Exp Fluids 38(5):695–699

Winter K (1979) An outline of the techniques available for the measurement of skin friction in turbulent boundary layers. Prog Aerosp Sci 18:1–57

Yan T, Jones B, Rakowski R, Tudor M, Beeby S, White N (2005) Metallic resonant strain gauges with high overload capability. Sens Rev 25(2):144–147